Research Square

Preprints are preliminary reports that have not undergone peer review.
They should not be considered conclusive, used to inform clinical practice,
or referenced by the media as validated information.

Impact of solvent vapor annealing on the electrical properties of electrochemical transistors

Soonseong Kwon
Chungnam National University
Seongbin Jo
Chungnam National University
Kihyon Hong
khong@cnu.ac.kr

Chungnam National University

Research Article

Keywords: Electrochemical transistors, solvent vapor annealing, surface morphology, specific capacitance, electrical performance

Posted Date: November 16th, 2026

DOI: https://doi.org/10.21203/rs.3.rs-11395793/v1

License: This work is licensed under a Creative Commons Attribution 4.0 International License.
Read Full License

Additional Declarations: No competing interests reported.

Impact of solvent vapor annealing on the electrical properties of electrochemical transistors

*Soonseong Kwon, Seongbin Jo, and Kihyon Hong**

Department of Materials Science and Engineering, Chungnam National University (CNU), Daejeon 34134, Republic of Korea

E-mail address: khong@cnu.ac.kr

ABSTRACT

Electrochemical transistors (ECTs) represent a specialized class of thin-film transistors utilizing ion-conducting electrolytes as gate dielectrics. Benefiting from substantial volumetric ion-doping and large interfacial capacitance, these devices achieve remarkable electrical characteristics, such as low operating voltage, elevated drain currents, and superior charge carrier mobilities. Consequently, extensive research has focused on identifying the primary factors governing ECT operation, ranging from ionic dimensions and transport kinetics within the electrolyte to the microstructural arrangement of the semiconducting layer. Although solvent vapor annealing (SVA) is routinely employed to optimize conventional organic field-effect transistors, its application in ECTs remains largely unexplored. Herein, we comprehensively examine how SVA modifies both the specific capacitance and semiconductor morphology in ECTs to clarify their respective roles in device operation. By employing SVA to tune these physical attributes, we reveal that the microstructural organization of the semiconductor; specifically, its degree of crystallinity, serves as the decisive factor determining

overall transistor performance. These findings clarify fundamental electrolyte-gating mechanisms and offer a practical design strategic for developing high-performance electrochemical electronics.

KEYWORDS

Electrochemical transistors, solvent vapor annealing, surface morphology, specific capacitance, electrical performance

1. Introduction

Electrochemical transistors (ECTs) constitute a distinct family of thin-film transistors (TFTs) incorporating an ion-conductive electrolyte alongside an ion-permeable polymeric semiconductor as the gate dielectric and active channel, respectively.[1-3] Fundamentally operating on the classical field-effect principle, ECTs modulate drain current (I_D) by accumulating charge carriers across the active channel when an external bias is applied. Under gate polarization, mobile ions within the electrolyte migrate to form electrical double layers (EDLs) across both the gate and channel regions. Because these EDLs are confined to a thickness of just a few nanometers, ECTs deliver extraordinarily large specific capacitances, typically spanning 1 to 500 $\mu F \cdot cm^{-2}$.[4-6] Concurrently, mobile ions can infiltrate the permeable polymer semiconductor, transforming the conductive pathway from a two-dimensional (2D) interfacial sheet into a three-dimensional (3D) volumetric channel.[4,7,8] This mixed ionic-electronic coupling drastically boosts carrier concentration throughout the film, enabling low-voltage operation (threshold voltage, $V_{th} < 3$ V), amplified output currents, and enhanced carrier mobility (μ).[9-11]

Because ECT operation relies on both interfacial EDL formation and bulk ion intercalation, the physical properties of the electrolyte, the semiconducting polymer, and their shared boundary directly govern electrical features. Numerous studies have sought to boost

ECT characteristics by tailoring key parameters, including ionic radius and diffusivity within the electrolyte, polymer chain packing, and volumetric capacitance. For example, employing smaller ions promotes deeper intercalation into the polymeric matrix, which elevates both I_D and μ.[12,13] Likewise, rapid ionic migration ensures swift switching dynamics and suppresses current-voltage hysteresis.[14] The crystalline architecture and topography of the active polymer film are equally vital, as highly ordered conjugated backbones establish continuous pathways for charge transport while minimizing carrier trapping and scattering.[10,15] Furthermore, maximizing specific capacitance allows a greater density of mobile charges to accumulate within the channel, lowering V_{th} and enhancing I_D. [4,16] Nevertheless, while solvent vapor annealing (SVA) is a widely adopted post-processing technique for improving conventional polymer field-effect transistors (FETs), its impact on the coupled ionic-electronic behavior of ECTs has rarely been investigated.

Herein, we explore how SVA post-treatment influences the operational mechanisms and electrical output of ECTs utilizing regioregular poly(3-hexylthiophene) (P3HT) as the active p-type channel. In particular, we closely examine the interplay between SVA-induced morphological evolution in the P3HT layer and the resulting variations in specific capacitance (C_{SP}). Exposing spin-cast P3HT films to solvent vapors triggers molecular self-assembly, which simultaneously alters the film's permeability to electrolyte ions and modulates C_{sp}. We characterized the topographic and crystallographic evolution of SVA-treated P3HT layers *via* X-ray diffraction (XRD) and atomic force microscopy (AFM), correlating these structural metrics directly with transistor parameters. Remarkably, although SVA treatment reduces the device C_{sp}, it substantially elevates the hole mobility from 1.70 to (2.1-3.2) $cm^2V^{-1}s^{-1}$. This performance gain stems from improved microstructural ordering and interconnected percolation pathways within the P3HT film, which facilitate efficient charge carrier transport. Overall, our study confirms that SVA is a highly effective approach for optimizing ECTs and

demonstrates that semiconductor crystallinity outweighs specific capacitance in governing carrier transport, offering a clear framework for engineering advanced electrochemical devices.

2. Experimental

2.1 *Materials and Reagents*

Electronic-grade regioregular P3HT (4002−EE) was obtained from Rieke Metals. Heraeus supplied the aqueous dispersion of conductive poly(3,4–ethylenedioxythiophene):poly(styrene sulfonate) (PEDOT:PSS, Clevios PH 1000). Sigma-Aldrich provided chloroform, tetrahydrofuran (THF), toluene, the ionic liquid 1–ethyl–3–methylimidazolium bis(trifluoromethylsulfonyl)imide ([EMIM][TFSI]), and the copolymer poly(vinylidene fluoride-co-hexafluoropropylene) (P(VDF-HFP), average molecular weight M_n = 1.3 $\times 10^5$ g/mol).

2.2 *Preparation and Structural Characterization of P3HT films*

P3HT samples were deposited *via* standard spin-casting onto oxygen-plasma-treated Si/SiO_2 wafers. A precursor solution of P3HT dissolved in chloroform (concentration: 3 mg/mL) was dispensed and spun at 3,000 rpm. To perform the SVA treatment, the as-cast films were placed on a heated stage inside an enclosed glass chamber (diameter: 15 cm; height: 5 cm) alongside a small Petri dish (diameter: 2 cm; height: 0.8 cm) holding 3 mL of either chloroform, THF, or toluene, and maintained at 80 ºC for 60 min. To ensure reproducibility across measurements, the prepared samples were cut into several pieces, each 10 mm in length; this allows us to investigate the effects of different processing conditions on films originating from the same wafer. Surface topography and root-mean-square (RMS) surface roughness were evaluated *via* tapping-mode AFM (CoreAFM, Nanosurf), while crystalline ordering was probed using a Bruker Phase 8 diffractometer (XRD).

2.3 *Device Fabrication and Electrical Measurements*

Top-gate, bottom-contact ECTs were constructed on p-type silicon substrates coated with a thermally grown 300-nm-thick SiO_2. Source (S) and drain (D) electrodes consisting of Cr (5 nm) and Au (35 nm) were thermally evaporated through a shadow mask to define a channel length (L) of 100 μm and a width (W) of 1,000 μm. Prior to P3HT coating, the patterned substrates were sequentially sonicated in acetone and isopropanol, rinsed thoroughly with deionized water, dried under a nitrogen gas, and treated with O_2 plasma for 60 s. The P3HT solution was then spin-cast at 3,000 rpm and subjected to the SVA protocol described above. Subsequently, a solid-state ion-gel dielectric was laminated directly over the P3HT channel; this gel was prepared by co-dissolving P(VDF-HFP), [EMIM][TFSI], and acetone at a 1:4:9 weight ratio. Device assembly was completed by laminating a freestanding PEDOT:PSS gate electrode atop the ion-gel layer (**Supporting Information, Figure S1**). Electrical characterization was performed in the dark under ambient air using a precision source/measure unit (B2902A, Keysight), with at least eight individual transistors evaluated per condition.

3. Results and Discussion

3.1 Crystalline ordering and surface topography of P3HT films

Following spin-casting, the P3HT layers underwent SVA processing using chloroform (CF), tetrahydrofuran (THF), or toluene to systematically vary film microstructure and device C_{SP}. Given the Hildebrand solubility parameter of P3HT (δ = 9.5 $cal^{1/2}$ $cm^{-3/2}$), CF serves as a good solvent with minimal mismatch ($\Delta\delta$ = 0.2), whereas toluene behaves as a marginal solvent ($\Delta\delta$ = 0.6).[17,18] Exposing the polymer films to these distinct solvent vapors promotes controlled vapor sorption, plasticizing the matrix and mobilizing the P3HT backbones toward thermodynamically favored arrangements. A control film annealed solely in ambient air (Air-P3HT) was prepared as a baseline reference. Surface profilometry (Alpha-Step) indicated that all resulting polymer layers had thicknesses ranging from 70 to 100 nm. Low-magnification optical microscopy verified uniform coverage across the 1 cm × 1 cm substrates without

macroscopic pinholes or dewetting (**Supporting Information, Figure S2**). Next, we evaluated the water contact angle (WCA). The surface energy of P3HT is a key consideration because the interfacial properties at P3HT/electrolyte and P3HT/S-D electrode interfaces directly affect the performance of ECTs. Thus, we performed WCA measurement for the P3HT films, and results are shown in **Figure S3**. All specimens displayed comparable WCA values ranging from 78° to 81°, confirming that SVA processing negligibly alters macroscopic surface energy or interfacial wetting.

Crystallographic modifications induced by the solvent vapors were examined *via* out-of-plane XRD (**Figure 1**). The baseline Air-P3HT specimen displayed a faint diffraction feature near $2\theta = 5.6°$, assigned to the (100) lamellar reflection arising from interdigitated hexyl side chains [19,20]. In contrast, all SVA-processed films exhibited a pronounced amplification of this (100) reflection. This intensification confirms that absorbed vapor molecules increase free volume within the polymer matrix, facilitating chain self-assembly and periodic lamellar stacking.[21] Notably, the toluene-annealed film (toluene-P3HT) produced the strongest (100) diffraction peak while retaining a relatively broad full-width at half-maximum (FWHM). This distinct structural signature stems from the restricted swelling imposed by toluene vapor. Because P3HT exhibits limited solubility in toluene (~0.7 mg/mL), the infiltrating vapor molecules constrain long-range chain diffusion, which prevents the coarsening of large, defect-free crystallites and accounts for the broad FWHM.[22] Instead, this limited chain mobility triggers widespread, simultaneous nucleation throughout the bulk film.[23,24] Consequently, a dense network of highly edge-on orientation can be formed. This highly localized rearrangement effectively consumes the amorphous regions, maximizing the total volume fraction of the crystalline domains, thereby yielding the highest diffraction intensity.

Nanoscale surface topography was investigated *via* tapping-mode AFM over a 2.5 μm × 2.5 μm scan area (**Figure 2a–h**). The baseline Air-P3HT film exhibited a comparatively rough topography with an RMS roughness value of 2.3 nm. Conversely, SVA processing smoothed

the polymer surface, lowering the RMS roughness to 0.8–1.5 nm (Figure 2i) as solvent-assisted chain relaxation leveled surface asperities. This reduced RMS is ascribed to the molecular chain rearrangement during the SVA process. Note that the average grain size of CF-P3HT is larger than that of the other samples. (Figure 2j). Because CF is a highly compatible solvent for P3HT, its vapor induces extensive film swelling and rapid chain diffusion, promoting Ostwald-like crystallite coarsening and larger domain dimensions [25].

3.2 Electrical properties of ECTs with SVA-treated P3HT films

To evaluate how these structural differences affect transistor operation, we fabricated and characterized ECTs incorporating the variously treated P3HT channels. Before measuring standard current–voltage sweeps, we quantified the specific gate capacitance (C_{SP}) *via* transient discharge current integration (**Supporting Information, Figure S3**).[26] In this procedure, a holding gate bias between −0.1 and −0.4 V was applied to fully charge the channel, after which the bias was abruptly stepped to 0 V while recording the transient discharging current. Integrating these current transients yielded the accumulated areal charge density, and C_{SP} was determined from the linear slope of charge density plotted against gate bias (**Figure 3**a–d). Notably, all SVA-treated ECT displayed reduced charge accumulation and a lower C_{SP} compared to the baseline device (Figure 3e). This capacitance reduction directly reflects the denser molecular packing achieved during vapor annealing. Because the untreated Air-P3HT film possesses a largely disordered, loosely packed matrix, mobile anions from the ion gel readily infiltrate the bulk polymer, generating a high volumetric charge density and a large C_{SP} (137.5 μF/cm²). Conversely, vapor annealing drives polymer recrystallization into tightly packed lamellar domains that act as physical barriers to ionic diffusion, restricting bulk ion uptake and lowering C_{SP}. Moreover, the smoother topography of the SVA-treated layers (Figure 2) reduces the effective interfacial contact area with the laminated ion gel, further limiting ion injection into the channel.

At first glance, one might anticipate that the diminished charge density and reduced C_{SP} caused by SVA would degrade overall transistor output. However, the concomitant improvement in crystalline order dramatically accelerates hole transport, more than compensating for the loss in capacitance. **Figure 4a–d** presents the transfer curves (I_D–V_G) of the fabricated ECTs, all of which exhibit typical *p*-type accumulation behavior, sub-0.6 V operation, and high on-state drain currents exceeding 10^{-4} A—hallmarks of electrolyte-gated operation.[4,5,27] Beyond elevating the on-state current, SVA processing noticeably suppressed both the off-state leakage current and the forward/reverse sweep hysteresis. Although clarifying the exact mechanism warrants further investigation, this stabilization likely arises from the desorption of residual moisture and trapped oxygen species during heated solvent vapor exposure.[28] Threshold voltages (V_{th}) across all configurations remained tightly grouped between −0.14 and −0.01 V (**Supporting Information, Figure S4**). Correlating the AFM topography (Figure 2d) with the capacitance data (Figure 3), the slightly more negative V_{th} observed for the CF-ECT stems from its large, densely packed crystalline grains, which impede initial ion intercalation and require a slightly higher gate overpotential to initiate channel conduction. The corresponding output curves (I_D–V_D, Figure 4e–h) display clear gate-modulated current saturation at higher drain biases alongside strictly linear behavior at low V_D, confirming barrier-free ohmic hole injection from the Au contacts into the P3HT channel.

Figure 4i and 4j compare the peak transconductance (g_m) and hole mobility (μ) extracted from the transfer characteristics using the linear-regime relation $dI_D/dV_G = (W/L)\cdot\mu\cdot C_{SP}\cdot V_D$.[15] All vapor-annealed transistors outperformed the baseline Air-ECT (g_m = 0.57 mS, μ_{avg} = 1.7 cm²/V·s), achieving elevated transconductances of 0.92–1.24 mS and enhanced hole mobilities spanning 2.1–3.2 cm²/V·s.

Despite the decrease in capacitance resulting from the SVA treatment, the transconductance and mobility features of the ECT were obviously enhanced. This seemingly contradictory result, where the capacitance effect and the crystallinity effect compete, can be

effectively interpreted by understanding the fundamental electrolyte gating principle and electrochemical doping effect. While the solvent vapor induces a dense and ordered crystalline network (as shown in XRD and AFM results), it inevitably reduces the amorphous region and the number of interstitial sites available for ions to intercalate. Therefore, this restricted ion penetration leads to a measurable decrease in the C_{SP}. However, the influence of this capacitance reduction on the device performance is strictly linear and relatively marginal.

In stark contrast, the improved device transconductance and mobility driven by the enhanced crystallinity dictates the device performance on an exponential scale. In the Air-P3HT, the amorphous-like nature provides abundant sites for ion intercalation (yielding high C_{SP}) but lacks interconnected pathways for carrier transport, leaving the induced charge carriers trapped. By employing SVA, the resulting closely packed polymer chain network forms robust macroscopic percolation pathways. This structural evolution effectively overcomes the hopping energy barriers between chains, leading to an exponential surge in carrier mobility. (**Figure 5**) From this, we can conclude that semiconductor morphology is the primary dominant factor determining device performance.

4. Conclusion

To summarize, we comprehensively explored how post-deposition SVA processing governs the structural evolution of P3HT channels and the resulting electrical characteristics of ion-gel-gated ECTs. Combined XRD and AFM characterizations confirmed that exposure to solvent vapors promotes polymer chain self-assembly, substantially improving molecular crystallinity and surface smoothness. Because these tightly packed crystalline domains impede bulk ion intercalation, SVA processing reduces the specific capacitance of the transistors by up to 45% (from 137.5 to 75.0 μF/cm²). Despite this capacitance penalty, SVA treatment elevated the average hole mobility from 1.7 cm²/V·s to 2.1–3.2 cm²/V·s and more than doubled the transconductance. Thus, the superior electronic transport enabled by a well-ordered crystalline

network decisively outweighs the reduction in volumetric capacitance. This inverse relationship between ionic capacitance and electronic mobility demonstrates that semiconductor crystallinity acts as the primary determinant of overall ECT performance, establishing SVA as a simple yet powerful tool for optimizing electrolyte-gated organic electronics.

FIGURES

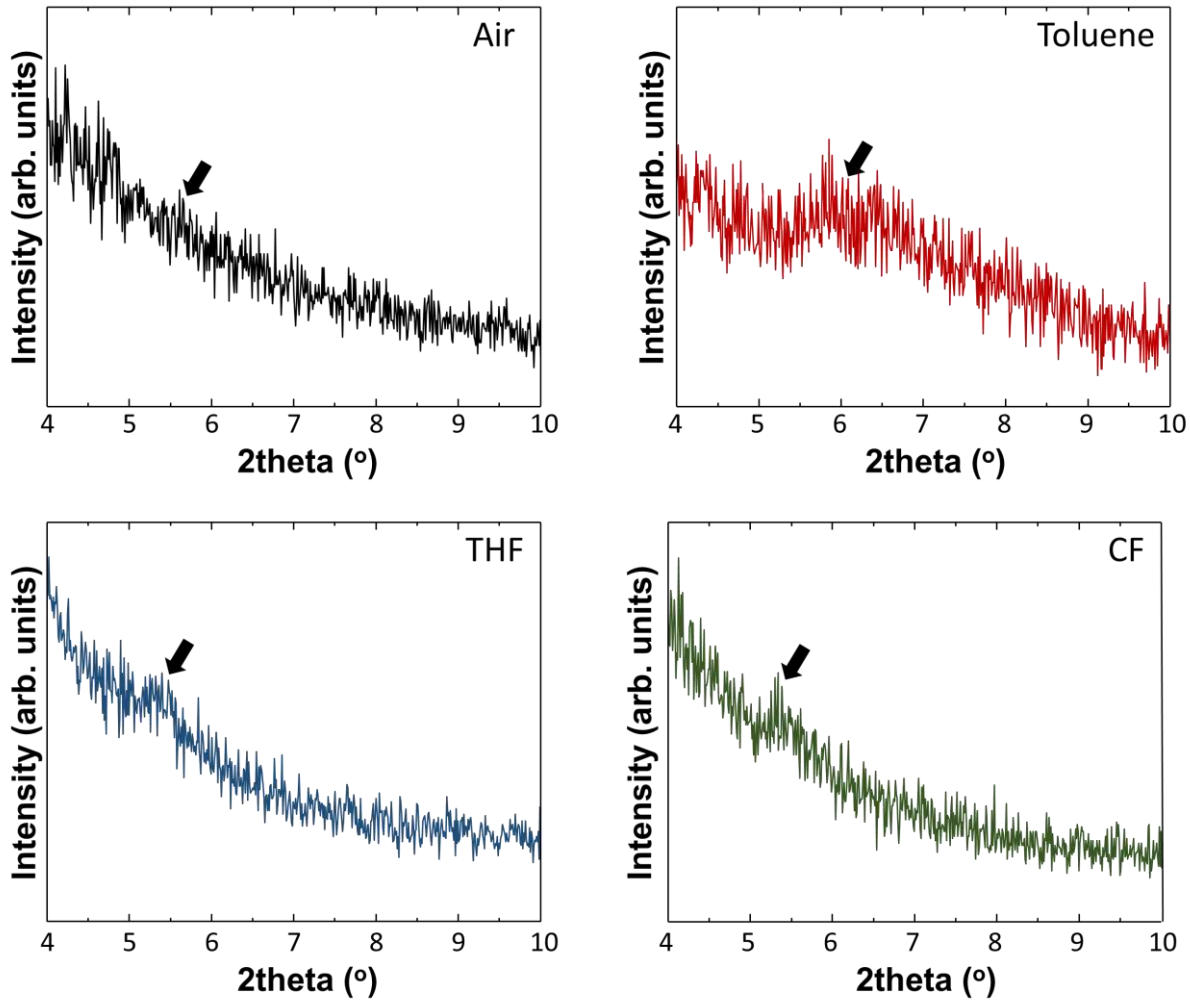


Figure 1. XRD spectra of P3HT samples. The arrows indicate (100) characteristic peak positions for each sample.

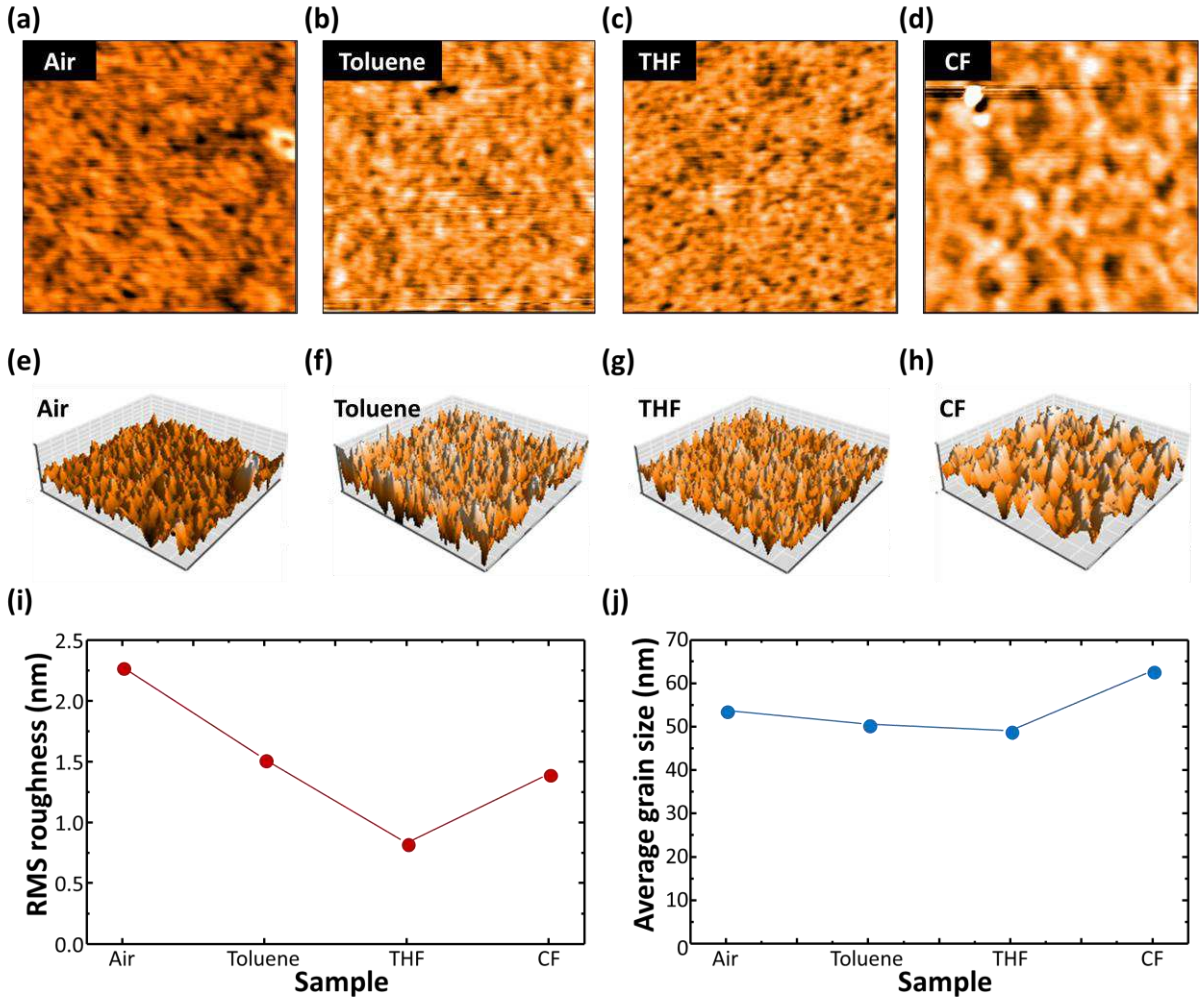


Figure 2. AFM (a-d) 2D-height and (e-f) 3D images of P3HT films with varying SVA solvents. The scan area is 2.5 μm × 2.5 μm. Change of (i) RMS roughness and (j) grain size of samples.

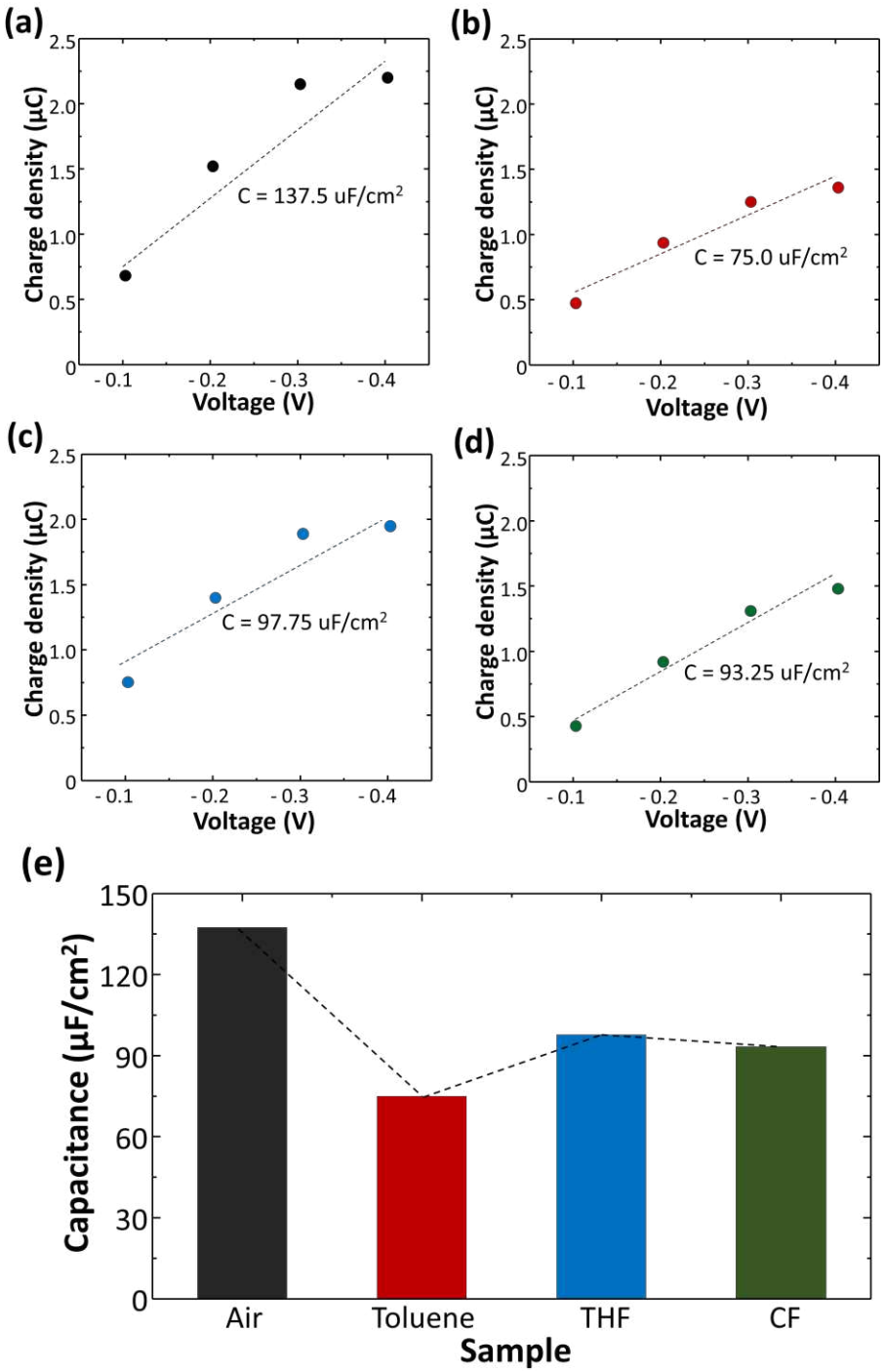


Figure 3. (a)-(d) Charge density versus voltage plots for ECTs as a function of SVA solvents. (e) Specific capacitances of ECTs with various SVA solvents. The values were extracted from the slope of charge density-voltage plots.

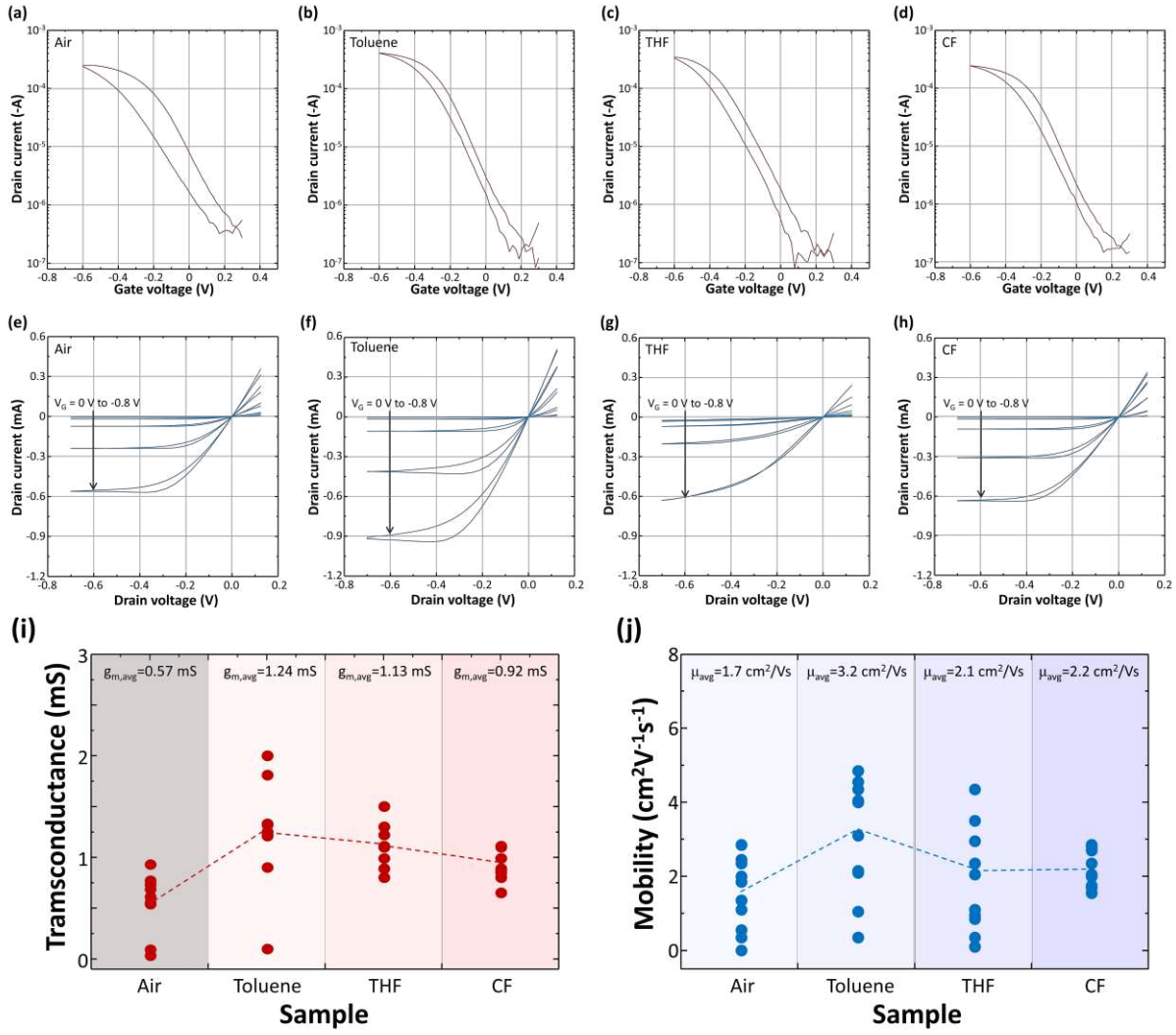


Figure 4. (a-d) Transfer and (e-h) output curves for ECTs with various P3HT films as channel layers. V_D is -0.1 V. Static distribution of (i) transconductance (g_m) and (j) device mobilities of 8 – 12 devices.

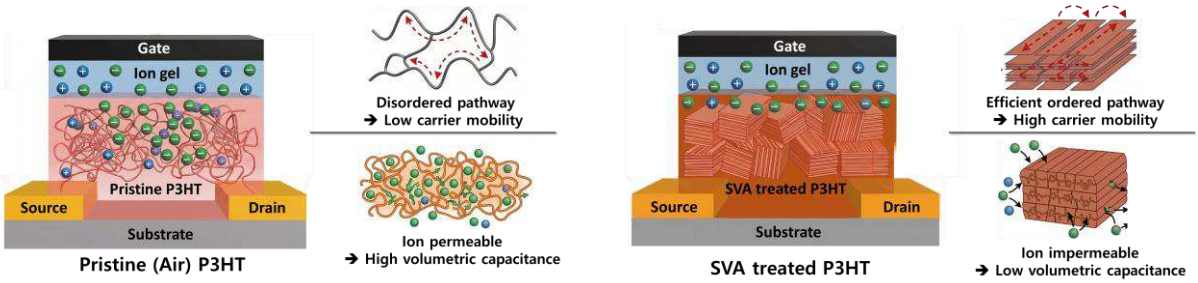


Figure 5. Schematic depicting the effect of crystallinity of P3HT and specific capacitance of ECTs on the electrical performance of transistors.

Acknowledgements

SK and SC contributed equally to this work. This work was supported by the National Research Foundation of Korea(NRF) grant funded by the Korea government (MSIT) (RS-2026-25484868)

Statements & Declarations

Funding

This work was supported by the National Research Foundation of Korea(NRF) grant funded by the Korea government (MSIT) (RS-2026-25484868)

Competing Interests

The authors declare no competing financial interest.

Ethical approval

The authors declare that the present works does not involve any human and animal involvement in the study and all the ethical standards are adapted and followed to carry out this work.

Author Contributions

S.K. and S.J. fabricated and characterized the ECT devices and also characterized the P3HT samples (AFM, XRD), while K. H. designed and supervised the overall study. The manuscript was written through the contributions of all authors. All authors have given approval to the final version of the manuscript.

Data availability

Data sharing is not applicable to this article as no datasets were generated or analysed during the current study.

Supplementary data

Schematic of the fabrication of P3HT films and devices. Optical microscope images of P3HT samples. Discharge current results for ECTs with P3HT films. Changes of V_{th} of ECTs.

References

[1] J. Chen. W. Huang, D. Zheng, Z. Xie, X. Zhuang, D. Zhao, Y. Chen, N. Su, H. Chen, R. M. Pankow, Z. Gao, J. Yu, X. Guo, Y. Cheng, J. Strzalka, X. Yum T. J. Marks, A. Facchetti, Nat. Mater. 21 564 (2022).

[2] X. Teng, J. Sun, J. Jiang, S. Ke, J. Li, Z. Lou, Y. Hou, Y. Hu, F. Teng, Org. Electron. 120, 106859 (2023).

[3] Y. Kuang, T. Yao, S. Deng, J. Dong, G .Ye, L. Zhang, S. Shao, Z. Zhu, J. Liu, J. Liu, Adv. Mater. 37, 2417691 (2025).

[4] S. H. Kim, K. Hong, W. Xie, K. H. Lee, S. Zhang, T. P. Lodge, C. D. Frisbie, Adv. Mater. 25, 1822 (2013).

[5] F. Torricelli, D. Z. Adrahtas, Z. Bao, M. Berggren, F. Biscarini, A. Bonfiglio, C. A. Bortolotti, C. D. Frisbie, E. Macchia, G. G. Malliaras, I. McCulloch, M. Moser, T.-Q. Nguyen, R. M. Owens, A. Salleo, A. Spanu, L. Torsi, Nat. Rev. Method. Prime. 1, 66 (2021).

[6] S. S. Awate, B. Mostek, S. Kumari, C. Dong, J. A. Robinson, K. Xu, S. K. Fullerton-Shirey, ACS Appl. Mater. Interfaces, 15, 15785 (2023).

[7] J. Rivany, S. Inal, A. Salleo, R. M. Owens, M. Berggren, G. G. Malliaras, Nat. Rev. Mater. 3, 17086 (2018).

[8] D. Ohayon, V. Druet, S. Inal, Chem. Soc. Rev. 52, 1001 (2023).

[9] W. Huang, J. Chen, Y. Yao, D. Zheng, X. Ji, L.-W. Feng, D. Moore, N. R. Glavin, M. Xie, Y. Chen, R. M. Pankow, A. Surendran, Z. Wang, Y. Xia, L. Bai, J. Rivany, J. Ping, X. Guo, Y. Cheng, T. J. Marks, A. Facchetti, Nature, 613, 496 (2023).

[10] M. Kim, S. Lee, K. Hong, Org. Electron. 145, 107306 (2025).

[11] K. G. Cho, S. J. Kim, D. H. Park, M. S. Kim, K. Hong, K. H. Lee, C. D. Frisbie, ACS. Appl. Mater. Interfaces, 17, 15718 (2025).

[12] K. G. Cho, K. H. Seol, M. S. Kim, K. Hong, K. H. Lee, ACS. Appl. Mater. Interfaces, 14, 50004 (2022).

[13] J. Sun, Y. Deng, J. Jiang, Y. Hu, Q. Cui, Z. Lou, Y. Hou, F. Teng, Org. Electron. 106, 106529 (2022).

[14] J. H. Cho, J. Lee, Y. He, B. Kim, T. P. Lodge, C. D. Frisbie, Adv. Mater. 20, 686 (2008).

[15] Y. Gil, Y. Jeong, K. Hong, ACS. Appl. Electron. Mater. 7, 158 (2025).

[16] J. Lee, L. G. Kaake, J. H. Cho, X.-Y. Zhu, T. P. Lodge, C. D. Frisbie, J. Phy. Chem. C. 113, 8972 (2009).

[17] J. Y. Oh, M. Shin, T. I. Lee, W. S. Jang, Y. Min, J.-A, Myoung, H. K. Baik, Y. Jeong, Macromolecules, 45, 7504 (2012).

[18] J. H. Park, J. S. Kim, J. H. Lee, W. H. Lee, K. Cho, J. Phys. Chem. C. 16, 101 (2019).
[19] F. V. Molefe, B. M. Mothudi, M. S. Dhlamini, Results Opt. 16, 100684 (2024).
[20] W.-H. Baek, H. Yang, T.-S. Yoon, C. J. Kang, H. H. Lee, Y.-S. Kim, Sol. Energy Mater. Sol. Cells, 93, 1263 (2009).
[21] J. H. Park, J. S. Kim, J. H. Lee, W. H. Lee, K. Cho, J. Phys. Chem. C. 113, 17579 (2009).
[22] E. Verploegen, C. E. Miller, K. Schmidt, Z. Bao, M. F. Toney, Chem. Mater. 24, 3923 (2012).
[23] H.-C. Liao, C.-S. Tsao, Y.-C. Huang, M.-H. Jao, K.-Y. Tien, C.-M. Chuang, C.-Y. Chen, C.-J. Su, U.-S. Jeng, Y.-F. Chen, W.-F. Su, RSC Adv. 4, 6246 (2014).
[24] S. Y. Shin, M. Jang, H. J. Cheon, S. Go, H. Yoon, M. Chang, Sens. Actuators B Chem. 351, 130951 (2022).
[25] S. Engmann, H. W. Ro, A. Herzing, C. R. Snyder, L. J. Richter, J. Mater. Chem. A. 4, 15511 (2016).
[26] Y. Ji, H. J. Lee, S. Lee, K. G. Cho, K. H. Lee, K. Hong, Adv. Mater. Interfaces, 6, 1900883 (2019).
[27] S. J. Kim, D. H. Park, Y. N. Lee, M. S. Kim, K. Hong, K. G. Cho, C. D. Frisbie, K. H. Lee,. NPJ Flex. Electron. 10, 44 (2026).
[28] L. A. Kehrer, S. Winter, R. Fischer, C. Melzer, H. von Seggern, Synth. Met. 161, 2558 (2012).

Supplementary Files

This is a list of supplementary files associated with this preprint. Click to download.

- P3HTSI.doc